A Fast and Robust Method for Predicting the Phase Stability of Refractory Complex Concentrated Alloys using Pairwise Mixing Enthalpy

Zhaohan Zhang[a], Mu Li[b], John Cavin[c], Katharine Flores[b,a], Rohan Mishra[b,a,*]

[a]Institute of Materials Science and Engineering, Washington University in St. Louis, St. Louis, MO, 63130, USA

[b]Department of Mechanical Engineering and Materials Science, Washington University in St. Louis, St. Louis, MO, 63130, USA

[c]Department of Physics, Washington University in St. Louis, St. Louis, MO, 63130, USA

Abstract

The ability to predict the composition- and temperature-dependent stability of refractory complex concentrated alloys (RCCAs) is vital to the design of high-temperature structural alloys. Here, we present a model based on first-principles calculations to predict the thermodynamic stability of multicomponent equimolar solid solutions in a high-throughput manner and apply it to screen over 20,000 compositions. We develop a database that contains pairwise mixing enthalpy of 17 refractory metals using density-functional theory (DFT)-based total energy calculations. To these, we fit thermodynamic solution models that can accurately capture the mixing enthalpy of multicomponent BCC solid solutions. By comparing their energy with DFT-calculated enthalpy of intermetallics from the Materials Project database and using convex hull analyses, we identify the stable phase of any RCCA as a function of temperature. The predicted stability of NbTiZr, NbTiZrV, and NbTiZrV*M* (*M* = Mo,Ta,Cr) systems as a function of temperature agree well with prior experimental observations. We apply our model to predict the phase evolution in NbVZr-Ti$_x$ ($0 < x < 1$), which is confirmed experimentally using a high-throughput, laser deposition-based synthesis technique. This method provides a fast and accurate way to estimate the phase stability of new RCCAs to expedite their experimental discovery.

1. Introduction

Multi-principal element alloys (MPEAs) are formed by mixing multiple elements at equiatomic or relatively high concentrations. A subset of MPEAs with ≥5 elements that form a single-phase solid solution are called high-entropy alloys (HEAs) [1, 2]. This new alloying strategy has vastly expanded the space of possible alloy systems and led to the discovery of MPEAs with properties not seen in conventional alloys [1, 3, 4]. Despite their compositional complexity, MPEAs tend to form random solid solutions in simple FCC, BCC, or HCP structures, partly due to the increase in configurational entropy with increasing number of elements, which reduces the Gibbs free energy of mixing. However, this "high entropy" effect is insufficient to counteract the driving forces that favor the formation of secondary phases [5]. In fact, among 670 unique MPEAs that were fabricated and characterized between 2004-2020 [6], only 33% of them form a single-phase solid solution or HEAs, while the remaining 67% comprise of coexisting solid solution phases and/or intermetallic phases. As the number of phases and their composition has a direct impact on the mechanical properties of the alloy [7, 8], the ability to rapidly predict the phase stability from the vast compositional space of possible MPEAs is a key step for accelerating their selection and deployment in applications. From a thermodynamic point of view, phase formation in MPEAs is determined by the minimization of total Gibbs free energy (ΔG), including both enthalpy and entropy contributions to the solid solution and any ordered intermetallics that may form for a given alloy composition. The formation enthalpy (ΔH_f) of binary and ternary intermetallics are nowadays readily accessible from computational databases, such as Materials Project, and machine learning models [9-11]; however, quantitatively predicting ΔH_f of random solid solutions having multiple elements and using them to eventually predict the phase formation in MPEAs remains a challenge.

To aid the selection of HEAs from the broader set of MPEAs, several approaches have been proposed. There are qualitative approaches that involve pairwise analyses of enthalpy and free energy for the constituent binaries within an MPEA to predict the stability of the solid solution [5, 12]. For instance, Troparevsky *et al.* developed a simple criterion to predict which elemental combinations are most likely to form an HEA by setting upper and lower bounds on ΔH_f of all ordered binary compounds that form for any given combination of elements [13]. Zhang *et al.* proposed a semi-quantitative approach for predicting the mixing enthalpy (ΔH_{mix}) of random solid solutions as the sum of pairwise interactions in the melts of their constituent binaries [14]. Specifically, for a *n*-component MPEA, they expressed $\Delta H_{mix} = \sum_{i=1,i\neq j}^{n} \Omega_{ij} x_i x_j$, where Ω_{ij} is the regular melt-interaction parameter, which is derived from the mixing enthalpy of i^{th} and j^{th} elements in binary liquid alloys using Miedema's model [15], and x_i is the concentration of i^{th} element. In combination with empirical descriptors, such as the difference in the atomic sizes of the constituent elements, it can separate MPEA compositions that are expected to form solid-solutions from amorphous phases [16]. A more accurate and quantitative method is to directly calculate the total energy of the solid solution using first-principles density-functional theory (DFT) calculations. This requires simulating the random configuration in multicomponent solid solutions using either large supercells of special quasi-random (SQS) structures [17-19] or numerous, small symmetry-inequivalent derivative structures [20, 21]; and calculating either of these using DFT is computationally expensive. Furthermore, the use of SQS to calculate the total energy of individual compositions makes it intractable to handle the large number of possible MPEAs. With regards to the use of derivative structures, Lederer et al. have taken a tour de force approach of using DFT to calculate the total energy of all possible *n*-atom/unit cell ($n \leq 8$) derivative structures for different combination of metals. They then fitted cluster expansion models to these derivatives to parameterize the interaction energies between different atoms and combined it with statistical thermodynamic models to identify temperatures at which a random solid solution is expected to be stable over decomposition into ordered compounds. Their model could correctly predict known solid-solution-forming equimolar binary, ternary, quaternary and quinary alloys, and their crystal structures, *i.e.*, FCC, BCC or HCP with very high accuracy (> 90 %). Despite this remarkable progress, it's rather computationally expensive to parametrize the miscibility-gap and solid solution boundary for a new system. Models that can quickly predict the phase stability for an equimolar MPEA at any given temperature, including the decomposition products — which can include a mixture of solid solution(s) and/or intermetallics — are needed to guide alloy selection and design.

Here, we present a model that can rapidly, and with high accuracy, predict ΔH_{mix} of equimolar ternary, quaternary, quinary and senary BCC solid solutions that form the class of refractory MPEAs and are popularly referred to as refractory complex concentrated alloys (RCCAs). The alloys involve 17 elements: Ti, V, Cr, Zr, Nb, Mo, Ru, Rh, Hf, Ta, W, Re, Os, Ir, Al, Si, and C. We obtain the ΔH_{mix} of the multicomponent solid solutions by combining DFT-calculated pairwise mixing enthalpies (ΔH_{ij}^{ss}, where i and j are different elements) of the constituent equimolar binaries with a regular solution model. Our predicted ΔH_{mix} of 48 equimolar BCC MPEAs show a mean absolute error (MAE) of 16 meV/atom compared to their values calculated directly using DFT with SQS models. We further combine the mixing enthalpy of the solid solutions with the formation enthalpy of intermetallics available in the Materials Project database[22], and use convex hull analyses to predict the most stable phase of ~20,000 equimolar BCC MPEAs at any given temperature with respect to their decomposition products, which can be a mixture of equimolar solid solution(s) and/or intermetallics. We also applied our method to predict the phase evolution in NbTiZr, NbTiZrV, and NbTiZrVM (M = Mo,Ta,Cr) equimolar systems and find the results to be in excellent agreement with experimental observations [7]. Finally, we use our model to predict the phase evolution in NbVZr-Ti$_x$ ($0 < x < 1$) and confirm the results using a high-throughput, laser-processed alloy library. We also note that a similar work was published by Bokas et al. recently [23], where the authors also used pairwise mixing enthalpies to predict the mixing enthalpy of multicomponent solid solutions with high accuracy. Together, these models offer a pathway to accelerate the discovery of multicomponent alloys with desired combination of solid solution and intermetallic phases.

2. Methodology

2.1. A model for predicting the mixing enthalpy of multicomponent BCC solid solutions

We propose that the pairwise mixing enthalpy, ΔH_{ij}^{ss}, obtained using a regular solution model can adequately describe the interactions in multicomponent solid solutions. We have used a hypothetical equimolar quaternary alloy of elements A, B, C and D to show the process of calculating its ΔH_{mix} from pairwise interactions. This process is shown schematically in Fig. 1(a). First, we employ SQS models to generate a series of supercells that approximate a disordered equimolar binary solid solution on a BCC lattice [17]. After testing with different sizes, we select a 24-atom supercell that has a minimal size and shows perfect match to a random alloy when considering 58 pairwise interactions up to the 5th nearest neighbor and 48 triplet interactions up to the 3rd nearest neighbor. Next, we calculate the mixing enthalpies of these binary random solid solutions (ΔH_{ij}^{ss}) with DFT. The computational details are provided in Section 2.3.

With the DFT-calculated ΔH_{ij}^{ss} of binary random alloys, we can derive the pairwise interaction parameters between a pair of elements using a regular solution model, as shown in Eqn. (1):

$$\Delta H_{ij}^{SS} = \Omega_{ij} x_i x_j, \tag{1}$$

where i and j represent two different elements that form the alloy, x_i and x_j represent their respective concentrations such that $x_i + x_j = 1$, and Ω_{ij} represents their interaction parameter. From Eqn. (1), we get the pairwise interaction parameter $\Omega_{ij} = \Delta H_{ij}^{ss}/(x_i x_j)$. Then, we estimate the mixing enthalpy (ΔH_{mix}) of the multicomponent BCC solid solutions with a symmetric regular solution model by only considering the interaction energy of the constituent pairs [24], as shown in Eqn. (2) for an *n*-component alloy and Eqn. (3) for the quaternary solid solution *ABCD*:

$$\Delta H_{mix} = \sum_{i=1, i\neq j}^{n} \Omega_{ij} x_i x_j, \tag{2}$$

$$\Delta H_{mix}(ABCD) = \Omega_{AB}.x_A x_B + \Omega_{AC}.x_A x_C + \Omega_{AD}.x_A x_D + \Omega_{BC}.x_B x_C + \Omega_{BD}.x_B x_D + \Omega_{CD}.x_C x_D. \tag{3}$$

As exemplified in Fig. 1(a), for a quaternary alloy *ABCD*, we estimate its mixing enthalpy by summing up $\Omega_{ij} x_i x_j$, where $i, j \in \{A, B, C, D\}$ and $i \neq j$ for all elemental pairs, as shown in Eqn. (3).

With this method, we have calculated ΔH_{ij}^{ss} of 136 equimolar binary alloys formed by the 17 elements that are highlighted in the Periodic Table in Fig. 1(b) and are frequently used in RCCAs. We plot a heatmap showing ΔH_{ij}^{ss} between each pair of elements in Fig. 1(c). A green shade indicates a negative value and suggests that the pair of elements favor mixing to form a BCC solid solution compared to their elemental state. A purple shade implies that the pair of elements need extra energy to mix in a BCC phase. A full database of ΔH_{ij}^{ss} is included in Appendix B.

2.2. Predicting the most stable phase(s) of equimolar RCCAs

We determine the most stable phase of RCCAs at any temperature by comparing the thermodynamic stability of competing phases involving all possible equimolar solid solutions and intermetallics. Specifically, for the prediction of RCCAs, which have a BCC crystal structure, we predict ΔH_{mix} of BCC solid solutions with different number of components using the model discussed above, and retrieve ΔH_f of binary and ternary intermetallics from the Materials Project database [10]. As most of the elements considered in this work exist in BCC phase, their alloys typically exist in the BCC phase; although there are exceptions [25, 26]. For such exceptional cases, the energy of the solid solution with FCC or HCP phase can also be expressed from the pairwise mixing enthalpy of their binary solutions in their respective FCC or HCP phase, and the phase having the lowest energy could be considered, as has been done recently by Bokas et al. [23].

We next consider the effect of temperature by calculating the Gibbs free energy, $\Delta G_{mix} = \Delta H_{mix} - T\Delta S$. For the BCC solid solutions, we consider the entropy as the ideal configurational entropy of mixing: $\Delta S = \Delta S_{config} = -k_B \sum_{i=1}^{n} x_i ln x_i$, where k_B is the Boltzmann constant, n is the number of elements, x_i is the concentration of i^{th} element and $\sum_{i=1}^{n} x_i = 1$. For the ordered intermetallic phases, ΔS is set to 0. Other entropy terms, such as vibrational entropy and electronic entropy, which are computationally expensive and are typically one or two orders of magnitude smaller then $T\Delta S_{config}$ [27, 28], have been neglected. Next, we utilize the convex hull analysis as implemented in pymatgen [29] to identify the stability of the BCC solid solution of the RCCAs with respect to decomposition products at any given temperature. The convex-hull construction evaluates the stability of a given phase against any linear combination of compounds that have the same averaged composition [30]. In the quaternary alloy $ABCD$ for instance, we compare its stability with respect to 3 equimolar ternary alloys (ABC, ABD, BCD) and 6 binary alloys (AB, AC, AD, BC, BD, CD), along with any binary or ternary intermetallics that are reported in the Materials Project database. We define this temperature above which the single-phase solid solution is stable as critical temperature T_c [31, 32]. Below T_c, phase decomposition is predicted and at least one element is no longer fully miscible in the solid solution. We apply this analysis to 680 ternary, 2380 quaternary, 6188 quinary, and 12376 senary equimolar refractory HEAs based on the 17 elements included in this study and compare some of the predictions with experimental observations.

We note here that the accurate determination of the thermodynamic phase stability at a given temperature requires not only direct comparison of Gibbs free energies, but also the curvature of Gibbs free energy curve for different phases [33, 34]. Ideally when multiple principal elements mix to form a single-phase BCC solid solution, at a specific temperature, the disordered BCC alloy is stable if it has both lower free energy than any decomposition products, and $\frac{d^2}{dx^2}\Delta G_{mix} > 0$. Curvature determination in high dimensions for multi-principal elements using first-principles calculations requires a dense compositional grid and is computationally intensive. Hence, to rapidly screen stable equimolar RCCAs, we only consider possible decomposition with equimolar sub-alloying compositions, unary metals and stable intermetallics as reactants. The solid solution phase is identified to be stable when it exhibits the lowest energy against the above decomposition reactions. For a specific alloy system of interest, we can employ our approach with dense composition grids taking non-equimolar alloys into account to determine its phase diagram[35], as we have discussed later in the Results section.

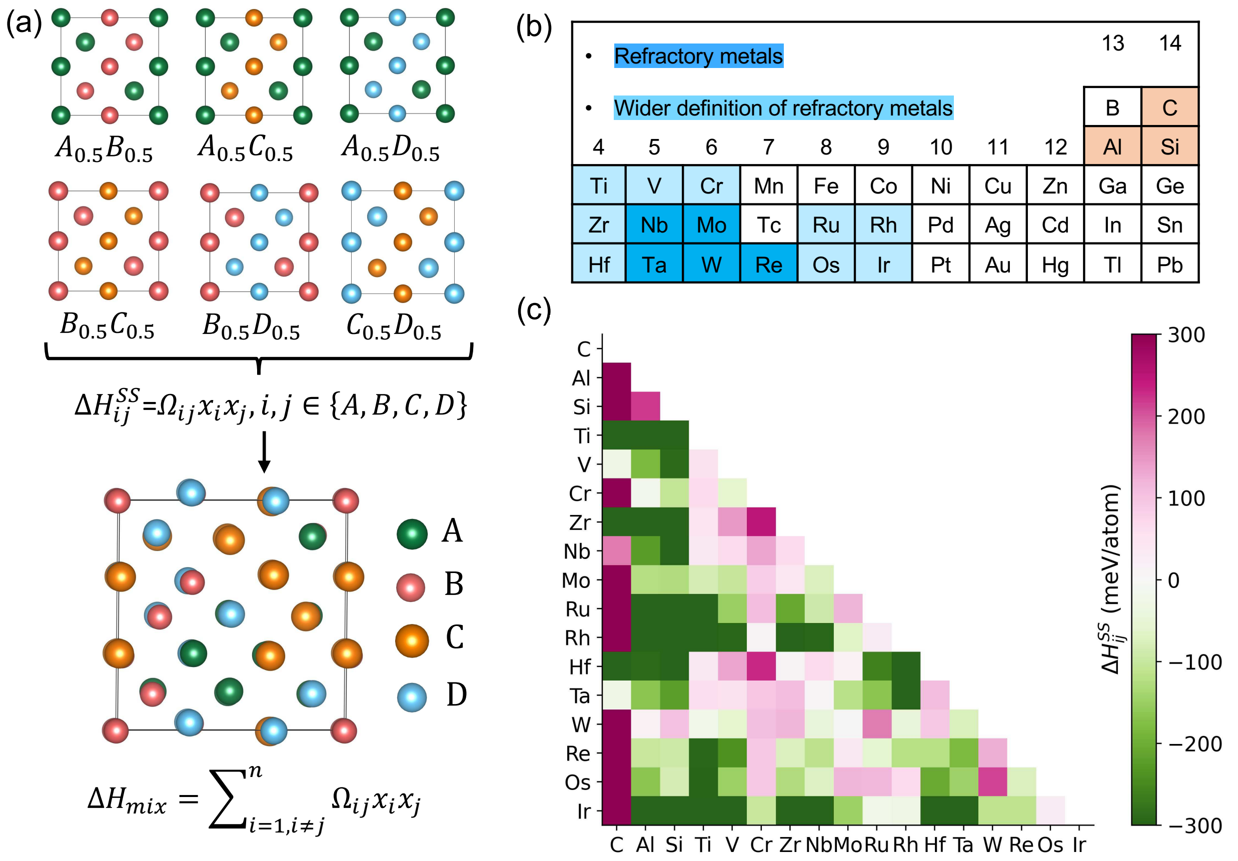

Fig. 1. (a) Schematic showing the approach we have used to calculate the enthalpy of mixing of a quaternary equimolar BCC solid solution of elements *A, B, C,* and *D* using their pairwise mixing enthalpy. (b) We calculate binary interaction parameters, Ω_{ij}, of 17 elements, including 5 refractory metals, 9 quasi-refractory metals and Al, C, and Si. (c) Heatmap showing the pairwise mixing enthalpy (in units of meV/atom) for the 136 pairs formed of the 17 elements.

2.3. Computational details

To model the disordered BCC solid solution, we generated SQSs [36] using the Alloy Theoretic Automated Toolkit (ATAT) [37]. For the high-throughput calculation of pairwise mixing enthalpy, we used a 24-atom supercell. For the simulation of ternary, quarternary and quinary alloys, we selected 36-atom, 48-atom, and 60-atom supercells, respectively [38]. We set the range of pair clusters to the 5th nearest neighbor and the triplets to the 3rd nearest neighbor. We performed first-principles DFT calculations using the Vienna Ab initio Simulation Package (VASP) [39]. We employed the generalized gradient approximation (GGA) as implemented in the Perdew-Burke-Ernzerhof (PBE) [40] exchange-correlation functional to approximate the many-body electronic interactions. We used the projector augmented-wave (PAW) method [41] to describe the core electrons with the outer p semicore states included as valence states. For the calculation of pairwise mixing enthalpy $\left(\Delta H_{ij}^{ss}\right)$, we fixed the plane-wave energy cutoff at 520 eV and relaxed the structures until the forces on each atom were less than 0.001 eV Å^{-1}. For the 24-atom supercell, a grid density of 10000 k-points/number of atoms was used. The binary ΔH_{ij}^{ss} is calculated with respect to constituent elements in their stable states ($E(i)$), as shown in Eqn. (4). ΔH_{mix} in multicomponent solid solutions were calculated in a similar manner. An example of ΔH_{mix} for a quaternary alloy is shown in Eqn. (5):

$$\Delta H_{ij}^{SS}(AB) = E(A_{0.5}B_{0.5}) - 0.5E_{el}(A) - 0.5E_{el}(B). \tag{4}$$

$$\Delta \mathrm{H}_{\mathrm{mix}}(ABCD) = E(A_{0.25}B_{0.25}C_{0.25}D_{0.25}) - 0.25E_{el}(\mathrm{A}) \text{- } 0.25E_{el}(\mathrm{B}) \text{- } 0.25E_{el}(\mathrm{C}) \text{- } 0.25E_{el}(\mathrm{D}). \tag{5}$$

2.4. Deposition of NbVZr-Ti$_x$ alloy library and its characterization

A 20 × 20 × 5 mm equiatomic NbVZr substrate was produced using arc melting and casting. The raw materials with purity ≥ 99.8 wt. % were melted on a water-cooled copper hearth in an argon atmosphere. The obtained buttons were flipped and remelted at least five times to improve compositional homogeneity prior to casing into a copper mold to produce a 20 × 20 × 5 mm plate. The composition libraries were prepared using an Optomec MR-7 Laser Engineered Net Shaping system (LENS$^{\mathrm{TM}}$). On the NbVZr substrate, a total of 16 patches, each sized 2 mm × 2 mm, were alloyed by injecting varying amount of Ti powder (-100+325 mesh, ⩾ 99.5 % purity) into a melt pool created by the moving laser to produce NbVZrTi$_x$ alloys (x = 0 – 1). The powder feed rates varied from 2.0 rpm to 3.5 rpm in increments of 0.1 rpm, while the laser power and travel speed were held constant at 250 W and 6.35 mm/s, respectively. Each single-layered patch consisted of 5 parallel laser tracks, and there was approximately 25% overlap between adjacent tracks. Subsequently, the patches in the library were remelted twice with a 250 W laser to ensure proper mixing between Ti and the substrate material. More detailed description of the library preparation can be found elsewhere [42].

The crystal structures were characterized on the polished library surface (plan view) using X-ray diffraction (XRD, Rigaku D-Max/A) with Cu-K$_\alpha$ energy. Diffraction angles between 20° and 100° (2θ) were collected with a step size of 0.02°. To eliminate the effect of the surrounding materials and isolate the patches with varying Ti content, a plexiglass mask with a tapered circular aperture (2 mm in diameter) was employed. The diffraction signal from the mask was subtracted from the overall XRD patterns. The microstructures of the patches were characterized using a field emission scanning electron microscope (SEM, JEOL JSM-7001FLV) operated at 15 kV accelerating voltage. Their composition was evaluated using an Oxford Aztec Live X-Max energy dispersive X-ray spectroscopic system (EDS).

3. Results

3.1. Prediction accuracy of ΔH_{mix}

To verify the accuracy of our method, we compare the model prediction to the ΔH_{mix} of 69 equimolar refractory HEAs with DFT-calculated values obtained using SQS models. Among the 69 investigated compositions, 37 of them are experimentally reported alloys that we collected from the literature [6, 43], while the rest are generated by randomly selecting combinations of the refractory metals used in this study. For each alloy, we plot the error in the model-predicted ΔH_{mix} with respect to the DFT-calculated value in the top panel for ternary compositions in Fig. 2(a), quaternary compositions in Fig. 2(b), and quinary compositions in Fig. 2(c). The alloy compositions are labeled at the bottom of each figure. The areas shaded yellow, blue and violet represent, respectively, 7 ternary, 15 quaternary and 15 quinary compositions that have been reported in literature [6, 43]. The compositions in the unshaded areas have been generated randomly. The mean absolute error (MAE) for ternary, quaternary and quinary alloys are 15, 17, and 22 meV/atom, respectively. The small MAE values demonstrate that our model shows good accuracy in predicting the ΔH_{mix}. 80% of the prediction falls within the error range between -25 to 25 meV/atom, as indicated by the area between the two horizontal green lines. For reference, the MAE of DFT-calculated ΔH_f with respect to experimental measurements is ~ 0.145 eV/atom for entries in the Materials Project database, when using the elemental DFT total energies as chemical potentials [44, 45].

In addition, we use the same alloy compositions to test the accuracy of the regular-melt model developed by Zhang et al. [14], which are shown in the middle panel in Figs. 2(a-c). In the regular-melt model, the mixing enthalpies of binary liquid alloys from Miedema's model (ΔH_{ij}^{liq}) [15] are used as fitting parameters. The MAE for ternary, quaternary and quinary compositions are 82, 83, and 83 meV/atom, respectively. We also repeat the analysis using the lowest formation enthalpy of stable binary intermetallics (ΔH_{ij}^{int}) that were collected by Troparevskey et al. from the AFLOW database[13, 46], which results in MAE of 116, 123, and 189 meV/atom for ternary, quaternary and quinary compositions, respectively. Thus, we find that combining DFT calculations done on binary alloys with a regular solution model gives accurate prediction of ΔH_{mix} in multicomponent solid solutions. The pairwise interactions obtained from a disordered BCC lattice, as opposed to liquid alloys or ordered intermetallics, are necessary for making accurate predictions. The simulation of binary solid solutions requires small 24-atom supercells and are less computationally intensive than directly modeling the multicomponent solid solutions, which will require (36-120)-atom supercell for ternary, quaternary, and quinary systems, not to mention the vast combinatorial composition space of those alloys, each of which will require a separate SQS. By constructing a binary ΔH_{ij}^{SS} database, we can efficiently screen a large number of multicomponent systems and assist the design of RCCAs. In this work, with only 136 computations on pairs formed by the 17 elements, we predict ΔH_{mix} of over 20,000 equimolar multicomponent compositions. We have made this repository available online [38].

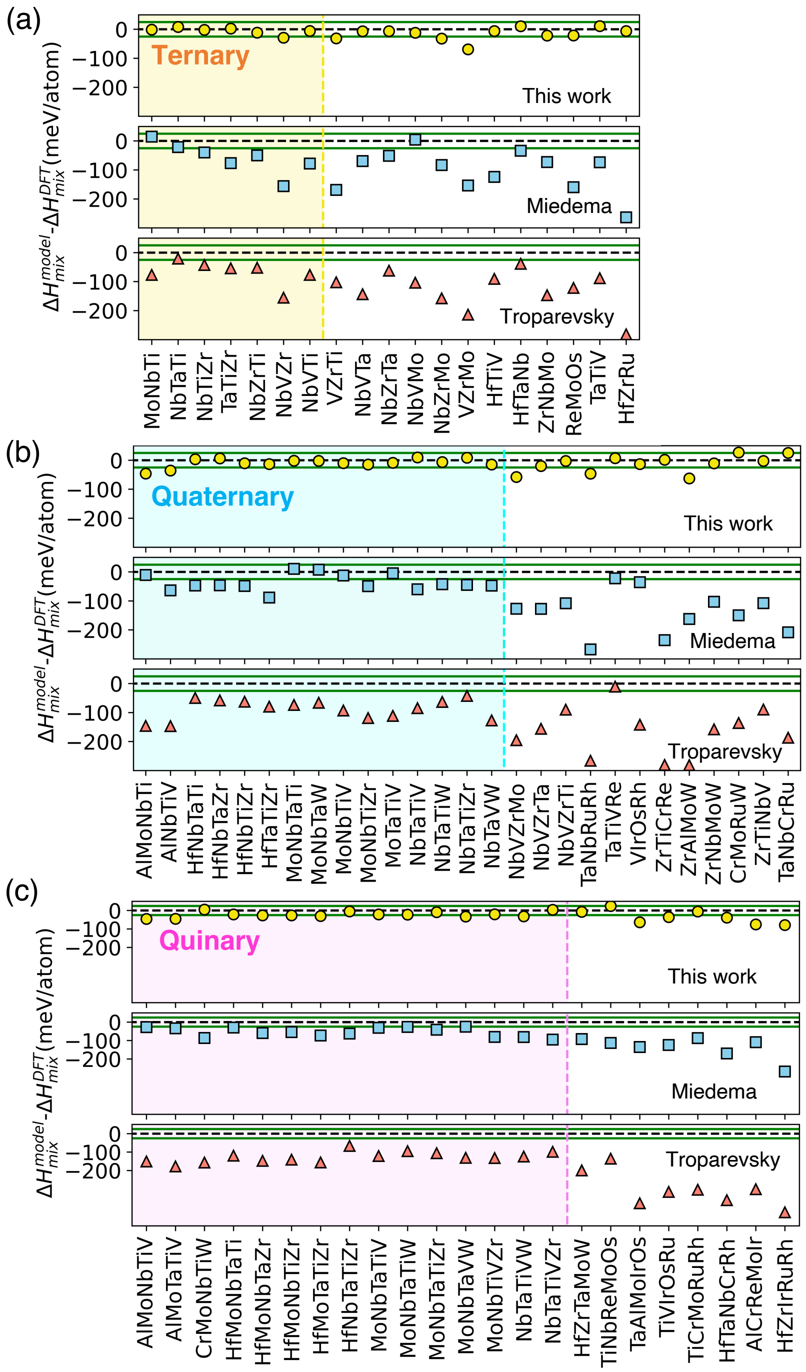

Fig. 2. A comparison of ΔH_{mix} predicted using regular solution models with their DFT-calculated value for (a) ternary, (b) quaternary, and (c) quinary equimolar RCCAs. For each alloy family, the top panel represents the predictions from this work, where the interaction parameters for the regular solution model were obtained using DFT-calculated pairwise mixing enthalpies (ΔH_{ij}^{SS}). The middle

panel shows results obtained using the mixing enthalpy of binary liquid alloys from Miedema's model (ΔH_{ij}^{liq})[15]. The bottom panel uses the formation enthalpy of binary intermetallics collected by Troparevsky et al. (ΔH_{ij}^{int})[13]. The *y*-axis shows the prediction error in units of meV/atom for each model. The two horizontal green lines in each panel indicate the range of errors between -25 to 25 meV/atom. The areas shaded yellow, blue and violet represent, respectively, 7 ternary, 15 quaternary and 15 quinary compositions that have been reported in literature [6, 43]. The compositions in the unshaded areas have been generated randomly.

3.2 Phase predictions validated by experiments

3.2.1 NbTiZr-based equimolar refractory HEAs

Having established that pairwise mixing enthalpies, ΔH_{ij}^{SS}, can predict ΔH_{mix} of multicomponent solid solutions with similar accuracy as DFT, we next compare our model prediction of phase evolution as a function of temperature for specific RCCAs where experimental observations are available. Here, we use NbTiZr-based RCCAs as a model system to demonstrate the convex hull analysis process and benchmark our predictions with experimental observations from Senkov et al. [7]. Starting with the ternary alloy NbTiZr, we first retrieve ΔH_{ij}^{SS} of the 3 constituent binary compositions NbTi, NbZr, and TiZr from our database, and use them to predict ΔH_{mix} of NbTiZr. We then query all binary and ternary entries that are reported in the Nb-Ti-Zr chemical space in the Materials Project database. In this case, we obtain 11 binary ordered compounds and 1 ternary compound, whose ΔH_f are all positive and range between 34 – 155 meV/atom, as shown in Table 2 in Appendix C. The ΔH_f of the three constituent elements, Nb, Ti, Zr, is set to 0 following Eqn. (4). We then calculate ΔG of all 19 phases by assuming ideal configurational entropy of mixing and conduct the convex hull analyses for temperatures ranging from 0 to 3000 K, in steps of 200 K. At each temperature, we assess the stability of a given phase versus its decomposition to any linear combination of possible phases that give the same average composition. A convex hull is determined by combining all stable phase points such that any linear combination of possible phases lies on or above the convex hull, i.e., have the same or higher ΔG. On the convex hull boundary, the energy curve is convex such that $\frac{d^2}{dx^2}\Delta G_{mix} \geq 0$. Therefore, we represent the stability of a phase by the term energy above hull (E_{hull}). If a phase is stable (i.e. on the convex hull), $E_{hull} = 0$; if not (i.e., it is above the convex hull), E_{hull} is positive and it will decompose into phases with lower energy. We plot E_{hull} as a function of temperature for NbTiZr alloy in Fig. 3(a). The regions shaded with different colors represent the ranges of temperatures wherein different combination of phases are the most stable, and the unshaded region shows the temperature range where the multicomponent BCC solid solution is most stable. At 0 K, we find that NbTiZr BCC solid solution is unstable with E_{hull} = 25 meV/atom. It is expected to separate into elemental Nb, Ti, and Zr. With increasing temperature, the increasing contribution of $-T\Delta S_{mix}$ reduces the Gibbs free energy of the ternary solid solution, as indicated by the yellow curve in Fig. 3(a). For temperatures > 1000 K, the NbTiZr solid solution becomes stable as it lies on the convex hull. Our results agree well with experimental observations after annealing at 1400 ℃ for 6 hours [7], where the alloying elements were observed to be homogeneously distributed in equiaxed BCC grains. We define this temperature above which the single-phase solid solution is stable as critical temperature T_c. We note that the temperature step we use here is 200 K, so T_c can have an error range $\pm$200K. Other neglected entropy terms, such as vibrational entropy, will also impact T_c.

Next, we investigate the phase stability in the quaternary system with the addition of V to NbTiZr. For the analysis of NbTiZrV, we construct the convex hull with 1 quaternary solid solution, 4 ternary solid solutions, 6 binary solid solutions, 4 unary metals, as well as the intermetallic entries, as shown in Table 3 in Appendix C. We predict the quaternary alloy to stabilize as a single-phase BCC solid solution, i.e., $E_{hull} = 0$, above 1400 K, as indicated by the green curve in Fig. 3(b). At lower temperatures, the most stable phases comprise of a NbTiZr-rich BCC phase and a NbV$_2$-rich Laves phase. Experimentally, NbTiZrV is found to have a dominant BCC phases with clusters of fine, V-rich precipitates(22Nb-21Ti-18Zr-39V at.%) inside NbTiZrV grains [7], which is consistent with our prediction.

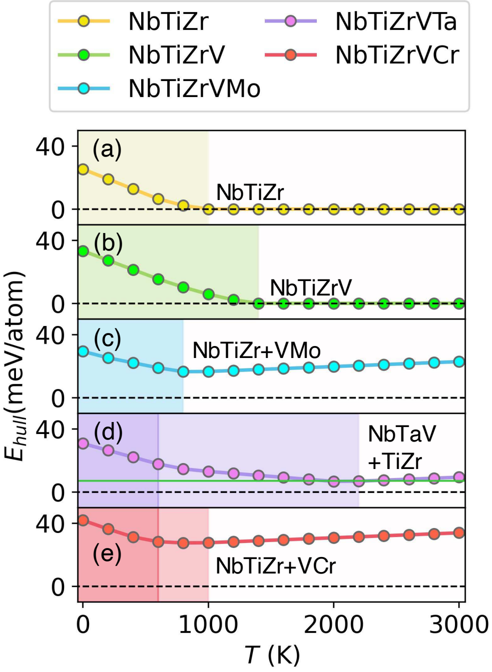

Fig. 3: Predicted phase stability of NbTiZr-based refractory HEAs. (a) NbTiZr and (b) NbTiZrV single-phase BCC solid solutions become stable at 1000K and 1400K, respectively; (c) NbTiZrVMo, (d) NbTiZrVTa, and (e) NbTiZrVCr are predicted to stabilize as two BCC phases at higher temperatures. The shaded areas in each panel

indicate the temperatures at which the ground-state phases include one or more intermetallics.

Further alloying of NbTiZrV with a fifth element, Mo, Ta or Cr introduces more possible phases that range from 5-component compositions to pure elements. For NbTiZrVMo, when the temperature ranges from (0 – 800) K, the most stable phases consist of MoTi-rich BCC, NbV_2-rich Laves and Zr-segregated phases, as shown by the region shaded in blue in Fig. 3(c). For temperatures >800 K, we predict the alloy to stabilize as two separate BCC phases, NbTiZr and MoV. In experiments, after homogenization annealing at 1400 ℃, NbTiZrVMo shows a dendritic microstructure consisting of three phases: Zr-depleted BCC-1, Zr-rich BCC-2, and $(Mo, V)_2Zr$ Laves phase [7]. Hence our thermodynamic model successfully predicts the two BCC phases at higher temperatures, while the Laves phase is captured at lower temperatures. The observation of Laves precipitates at high temperatures in experiments could be due to other thermodynamic factors, such as interface energy between the precipitates and the matrix, or kinetic factors such as the sluggish diffusion observed in many HEAs[47]. Our prediction agrees well with a first-principles study on NbTiZrVMo [48], where the authors investigated the short-range ordering in Nb-Ti-Zr-V-Mo system using Monte Carlo simulations, and also observed that Mo and V tend to cluster while Zr tends to separate from Mo and V.

We conducted a similar analysis on NbTiZrVTa and predict several phase transitions with temperature, as shown in Fig. 3(d). Each shaded area indicates a region where a different phase or combination of phases is most stable. From left to right, for temperature < 600 K, the stable mixture consists of a solid solution of NbTa that we call BCC1, a solid solution of NbTi or BCC2, TaV_2 Laves, and a Zr-segregated phase; for temperatures between (600 – 2200) K, the most stable phases are NbTiZr-BCC1, NbTa-BCC2, TiZr-BCC3, and TaV_2 Laves phases; and above 2200 K, the Laves phase is suppressed and the alloy stabilizes into NbTaV-BCC1 and TiZr-BCC2. For reference, the average melting temperature of these five elements is 2462 K. Experimentally, NbTiZrVTa consists of two BCC phases in hot-worked conditions and is a single-phase BCC solid solution after annealing at 1400 ℃ [7]. This discrepancy between our predictions and the experimental microstructure after annealing could be due to the very small value of $E_{hull} = 7$ meV/atom for the NbTiZrVTa BCC phase predicted using our model, which is below the MAE of 22 meV/atom for quinary systems. Furthermore, a positive energy is required for the nucleation of a secondary phase and the formation of interfaces between the product phases. Therefore, phases with small E_{hull} values, can be expected to be stable.

We notice similar phase transition trends in NbTiZrVCr. At low temperatures ranging from (0 – 400) K, it shows NbVCr clustering and segregation of Zr and Ti. From 600 to 1000 K, configurational entropy favors the mixing of NbTi and VCr, while Zr remains segregated. When the temperature goes above 1000 K, it stabilizes into NbTiZr-BCC1 and VCr-BCC2, as shown in Fig. 3(e). Experimentally, the annealed sample comprises of (Nb, Ti)-rich BCC1 and (V, Cr)-rich Laves, with Zr distributed in both the phases. Comparing the experimental microstructure with our prediction, we successfully capture the clustering tendency of Nb-Ti and V-Cr. However, the exact Laves phases were missed since we ignored the entropy stabilization effect at higher temperature for intermetallic phases, which will be discussed in Section 4.

3.2.2 Phase evolution in NbVZr-Ti$_x$ ($0 < x < 1$) alloys

We further apply our method to assist the design of microstructure in RCCAs using NbVZr as a base alloy. Equimolar NbVZr exhibits a dendritic microstructure consisting of a BCC solid solution, with two Laves structures forming in the interdendritic regions [43]. The secondary Laves phases have been reported to strengthen the alloy by acting as obstacles to dislocation motion. To investigate the effect of composition on the microstructure evolution in the NbVZr-base alloy system, we alloy it with Ti and predict the phase stability as a function of Ti concentration [49]. We first predict the energy of non-equimolar NbVZr-Ti$_x$ ($0 < x < 1$) alloys using a regular solution model, as shown in Eqn. (3), where $x_{\mathrm{Nb}} = x_{\mathrm{V}} = x_{\mathrm{Zr}} = \frac{1}{3+x}$, $x_{\mathrm{Ti}} = \frac{x}{3+x}$, and x is in the range of $[0, 1]$ with a grid spacing of 0.1. For every non-equimolar NbVZr-Ti$_x$ composition, we conduct convex hull analysis and plot E_{hull}, in the units of meV/atom, of the NbVZr-Ti$_x$ BCC phase as a function of x and temperature as a heatmap in Fig. 4(a). At 0 K, the quarternary alloy tends to decompose into NbV$_2$-rich Laves, and segregated Zr, Nb, and Ti phases. With increasing temperature, NbZrTi-BCC phase is then stabilized by configurational entropy, with the precipitation of NbV$_2$ Laves phase. Finally, the quaternary NbVZrTi$_x$ BCC phase becomes stable at elevated temperatures. The black dashed line in the heatmap demarcates the composition and temperature at which a single-phase BCC alloy becomes stable, i.e., its $E_{hull} = 0$. Below the dashed line, it forms as a multi-phase alloy that contains BCC and Laves phases. For the ternary NbVZr alloy, the critical temperature T_c, at which their BCC solid solution becomes stable, is quite high at 2400 K; with increasing Ti concentration, T_c decreases, which suggests that NbVZr-Ti$_x$ alloys would tend to stabilize as BCC solid solution with increasing Ti fraction.

To confirm this prediction, we fabricated a laser-processed NbVZr-Ti$_x$ library and characterized their crystal structures as a function of composition with X-ray diffraction. The results are as shown in Fig. 4(b), from which we can see that Ti addition reduces the Laves phase fraction and results in a single-phase BCC solid solution in equimolar NbVZrTi.

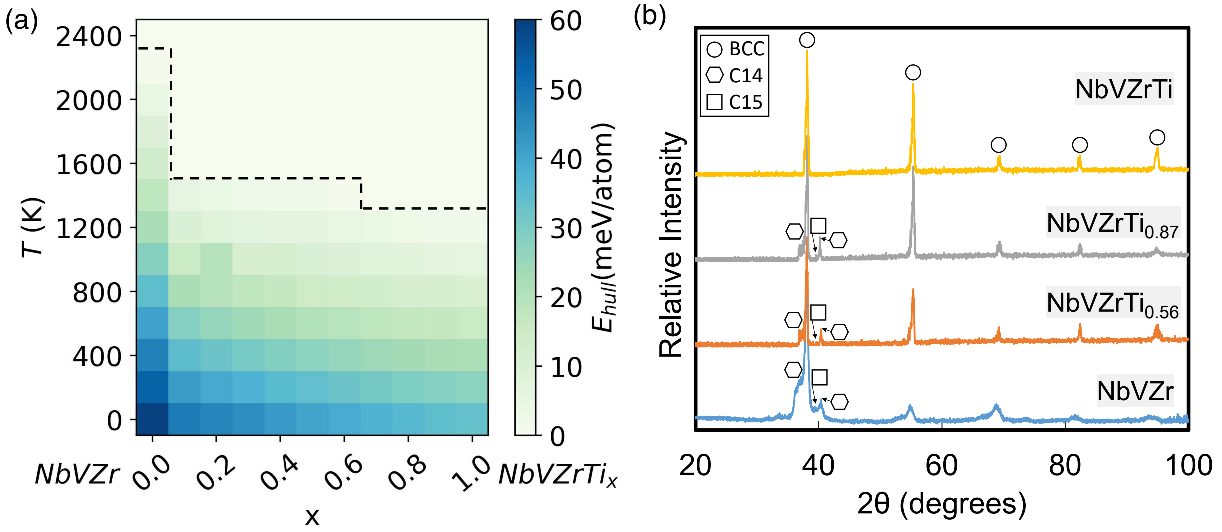

Fig. 4: Phase stability of NbVZr-based refractory HEAs: (a) Model-predicted BCC phase stability in $NbVZrTi_x$ $(0 < x < 1)$ alloys. The colormap indicates E_{hull} of $NbVZrTi_x$ as a function of Ti concentration, x, and temperature. When $E_{hull} = 0$, a single-phase BCC solid solution is stable. (b) X-ray diffraction of $NbVZrTi_x$ library. Ti addition eliminates the C14 and C15 Laves phases and results in a single BCC phase at equimolar composition.

3.3 Candidate RCCAs systems

With the above examples, we have shown that our model can predict the experimental phase-stability of both equimolar and non-equimolar RCCAs. We next apply it to identify new RCCA systems for future research. Here, based on the 17 elements in our dataset, we investigate the stability 680 ternary, 2380 quaternary, 6188 quinary, 12376 senary equimolar compositions. For each of them, we perform convex hull analyses comparing the energy of multicomponent BCC phase with all the lower order equimolar solid solutions and binary/ternary intermetallic phases retrieved from the Materials Project database. Using $E_{hull} = 0$ meV/atom as a standard for a stable phase, we plot the number of single-phase BCC RCCAs that are predicted at 1000 K and 2000 K, respectively, in the top panel of Fig. 5(a). We observe an overall reduced number of single-phase RCCAs with increasing number of elements due to the competing solid solutions and intermetallic phases introduced by the constituent elements. More single-phase RCCAs are stabilized at 2000 K compared to 1000 K as a result of the increase in configurational entropy at higher temperatures. Considering the energy required for the nucleation of secondary phases and the formation of interfaces during phase decomposition, we benchmark the metastability of the multicomponent BCC phase as $E_{hull} \leq 20$ meV/atom. This value is selected after comparing the E_{hull} of experimentally known single-phase RCCAs, as listed in Table 1 and shown in Fig. 6 in Appendix B. With this criterion, the number of synthesizable single-phase RCCAs increases, as shown in the bottom panel of Fig. 5(a).

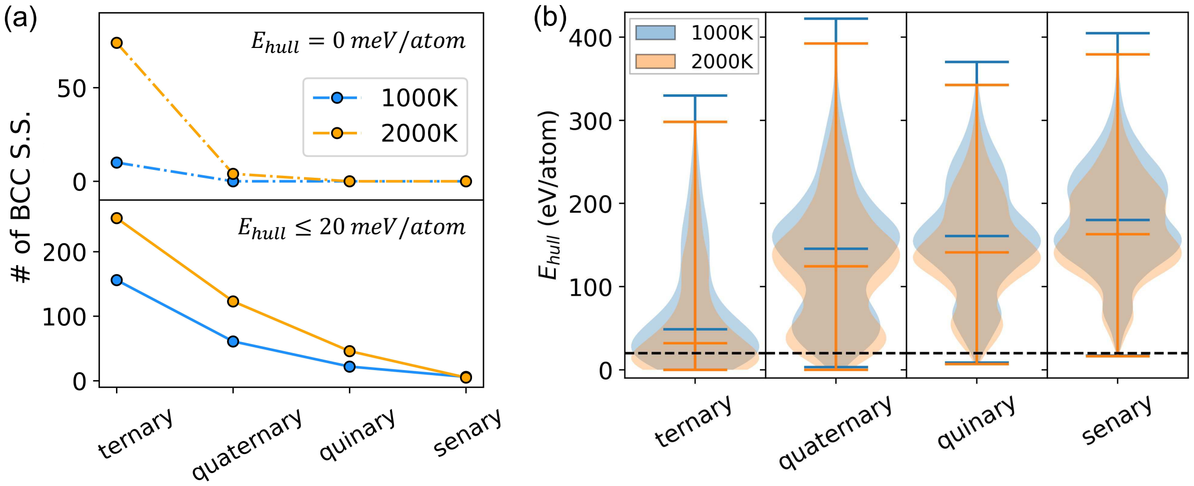

Fig. 5: (a) Number of RCCAs predicted to stabilize as a single-phase BCC solid solution out of the 680 ternary, 2380 quaternary, 6188 quinary, and 12376 senary equimolar alloys formed using the 17 elements used in this study. The results in the top panel were obtained with a stability criterion of E_{hull} = 0 meV/atom, and the ones in bottom panel were obtained using E_{hull} = 20 meV/atom. (b) The distribution of the predicted E_{hull} values for the BCC phase of all the multicomponent equimolar alloys in each of the four categories.

To visualize the relationship between the number of elements in RCCAs and their stability, we plot the distribution of E_{hull} for over 20,000 compositions in the category of ternary, quarternary, quinary and senary alloy systems, as shown in Fig. 5(b). In these violin plots, the lower, middle, and upper bars represent the minimum, median, and max E_{hull} values, respectively. We mark E_{hull} = 20 meV/atom with the black dashed line as the value for formability. The blue violin indicates predictions at 1000 K and the orange violin is for predictions at 2000 K. In each box, the orange violin shifts to lower E_{hull} values, signifying stabilization due to the increase in configurational entropy at higher temperatures. From left to right, we detect a shift of E_{hull} from lower to higher values. The fraction of compositions with $E_{hull} \leq 20$ meV/atom in ternary, quarternary, quinary, senary systems are 38.1%, 5.4%, 0.8%, and 0.1%, respectively, which shows that alloying with more elements does not necessarily lead to a single-phase solid solution. The formation of single-phase RCCAs requires a favorable mixing enthalpy of the constituent elements, as well as absence of a strong tendency for clustering — that can drive the formation of lower order solid solutions or intermetallics. With increasing number of constituent elements, the competing phases become more complex. In fact, even though the combinatorial chemical space is enormous with more elements, the percentage of alloys that favor formation of a single-phase drops dramatically, as shown in Fig. 5(a). We list the compositions that are predicted with $E_{hull} \leq 20$ meV/atom at 1000 K and 2000 K in the Appendix D. We have also shared the entire prediction dataset and example scripts to construct convex hull for specific alloy systems on a publicly available repository [38].

4. Discussion

The model we have developed can predict the stable phases and decomposition energies of a RCCA by using convex hull analyses. We show that it can successfully capture phase evolution observed experimentally in many refractory HEA systems. However, the current model does not include certain effects that may result in different outcomes. We list some of those factors below:

One factor is the value of E_{hull} below which a single-phase solid solution can be stabilized in experiments. When $E_{hull} = 0$ at a given temperature, the solid solution becomes the lowest energy phase. For positive values of E_{hull}, the system can lower its energy by decomposing into other stable phases. Yet, additional energy is needed for atoms to diffuse and for the nucleation of the secondary phase along with the formation of new interfaces. If the decomposition energy of the higher-order solid solution is not sufficient for the nucleation events, it is expected to be stable even though E_{hull} is positive. The energy scale for these complex processes can be estimated by comparing the E_{hull} of known single-phase RCCAs, as has been done for inorganic crystalline compounds by *Sun et al.* [50]. We have used the extremely limited set of 4 ternary, 15 quaternary and 15 quinary RCCAs, as listed in Table 1 in Appendix B, which have been characterized to form single-phase BCC alloy in experiments [6], and fit a Gaussian kernel density to their DFT-calculated E_{hull} value at 0 K. The resulting probability distribution for single-phase ternary, quaternary and quinary RCCAs as a function of their E_{hull} value is shown in Fig. 6 in Appendix B. While ternary and quaternary compositions show a metastability up to 20 meV/atom, quinary compositions exhibit higher metastability up to 50 meV/atom.

A second factor is the level of lower-order alloy systems included in the convex hull analyses. For the results presented above, we use the ground state energy of the constituent phases to identify thermodynamic equilibrium. That is, for an *N*-component system, we involve equimolar solid solution phases ranging from *N*-component, (N − 1)-component, …, to binary and unary, along with the intermetallic entries to determine the phase stability of equimolar RCCAs. We can instead use metastable decomposition products that may be observed in experiments due to limited interdiffusion, for example. This is especially relevant for certain combinatorial approaches for rapid alloy development [51], such as additive manufacturing. As an example, we compare the results of all-inclusive stability analysis with an analysis that only considers n-component versus (n-1)-component solid solution phases for 27 experimental quaternary alloys. All intermetallic phases are included in both the cases. The all-inclusive stability analysis predicts 10 of them to form single-phase solid solution with $E_{hull} = 0$, while the analysis that only considers decomposition into ternary solid solutions and intermetallic phases predicts 18 of them with $E_{hull} = 0$. Therefore, one can amend this parameter for the specific alloy fabrication method.

Lastly, we discuss the role of various entropy factors that were not included in our model. We assume that in the solid solution phases, the elements are randomly distributed and use the ideal configurational entropy of mixing for a fast assessment. This simplistic treatment is likely to miss effects such as short-range ordering that are frequently observed in experiments [8, 52]. This can be improved by using sub-regular solution models of mixing enthalpy that are fairly scalable [53, 54]. For greater accuracy, at the expense of speed, first-principles-based methods combined with molecular dynamics or Monte Carlo simulations can be used [55, 56]. We have also left out the entropy contributions in intermetallic phases by assuming that they are fully ordered. However, intermetallic phases in RCCAs usually have more constituents than sub-lattices, so that two or more elements will usually occupy one sub-lattice[57, 58]. For instance, consider an $L1_2$ phase in a quaternary alloy ($ABCDE$), if the intermetallic phase has a random distribution of elements A and B on one sub-lattice and a random distribution of elements C, D and E on the second sub-lattice, its configurational entropy will be equal to over 60% of the configurational entropy of the equimolar BCC solid solution $ABCDE$. In the future, we will include complex intermetallic phases and both the enthalpy and entropy contribution to refine our model. Moreover, we have excluded the contribution of vibrational enthalpy and entropy to the free energy of both the solid solution and the intermetallic phases. While the absolute magnitude of vibrational entropy (S_{vib}) can be much larger than configurational entropy, especially, at elevated temperatures [59, 60], the difference in vibrational entropy (ΔS_{vib}) between two phases having the same composition or between the parent and product phases, is often smaller than ΔS_{config} [61]. For instance, the vibrational free energies of the BCC and the Laves phases are nearly equal in CrMoNbV RCCAs [18]. Another study on a large set of binary alloys reported that the contribution of vibrational entropy to free energy is much smaller than that of configurational entropy for the majority of alloys studied in that work; however, in certain alloys with shallow mixing enthalpy, vibrational entropy had to be considered to accurately predict their miscibility. Thus, going forward, efficient approaches to calculate the vibrational free energy from first-principles calculations [62], followed by their parameterization, can make our model more accurate.

5. Conclusion

In summary, we present a fast and accurate thermodynamic method to predict the phase stability of RCCAs in a high-throughput manner. We show that pairwise mixing enthalpy is enough to give accurate prediction to the mixing enthalpy of multi-component solid solutions. Further, with convex hull analysis, we can construct phase diagrams of alloy systems that agree well with experimental observations. Finally, we screen over 20,000 RCCAs and investigate their thermodynamic stability at different temperatures. We propose our model to be a convenient tool to predict the phase stability of RCCAs and aid their experimental discovery. A python code to construct our model and the predicted datasets are available online [38].

Acknowledgements

This work was primarily supported by the National Science Foundation (NSF) under Grant No. DMR-1809571. J.C. and R.M. acknowledge support through NSF Grant No. CBET-1729787. This work used computational resources of the Extreme Science and Engineering Discovery Environment (XSEDE), which is supported by NSF through Grant No. ACI-1548562. The authors acknowledge financial support from Washington University in St. Louis and the Institute of Materials Science and Engineering for the use of shared instruments and staff assistance.

Appendix A. Pairwise mixing enthalpy database (unit: meV/atom)

	Mo	Nb	Ta	V	W	Zr	Ti	Al	Hf	Cr	C	Re	Ru	Os	Rh	Ir	Si
Mo	0																
Nb	-73	0															
Ta	-116	0	0														
V	-102	65	55	0													
W	-2	-41	-76	-59	0												
Zr	42	64	109	146	119	0											
Ti	-81	35	61	52	-21	49	0										
Al	-123	-223	-165	-183	14	-333	-307	0									
Hf	11	63	109	136	90	9	36	-290	0								
Cr	87	134	97	-60	106	251	65	-14	230	0							
C	373	176	-28	-30	504	-424	-340	460	-413	328	0						
Re	38	-113	-182	-238	126	-74	-295	-99	-120	92	810	0					
Ru	120	-91	-164	-149	173	-208	-321	-353	-260	109	698	-58	0				
Os	119	-68	-143	-147	212	-126	-296	-165	-206	92	944	-75	116	0			
Rh	-65	-294	-358	-294	-45	-546	-569	-655	-605	8	621	-121	28	65	0		
Ir	-146	-344	-422	-404	-111	-578	-656	-522	-639	-100	866	-111	-22	29	-30	0	
Si	-126	-301	-222	-291	102	-535	-411	220	-393	-103	354	-93	-326	-81	-552	-419	0

Note: The pairwise mixing enthalpy is calculated with respect to constituent elements in their stable states at T = 0K.

Appendix B. E_{hull} distribution for single-phase RCCAs

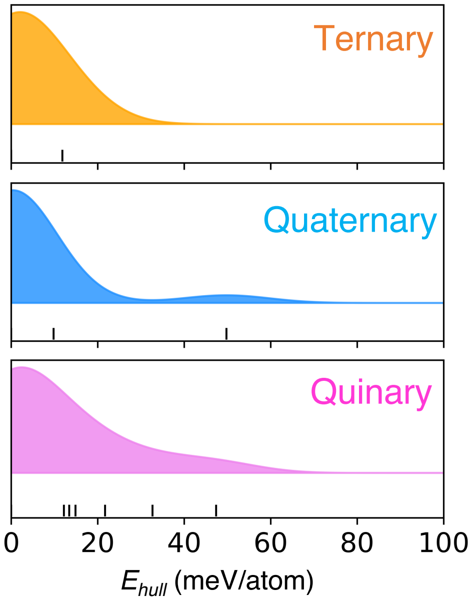

Fig. 6: Gaussian kernel density estimates of E_{hull} distribution for single-phase ternary, quaternary and quinary RCCAs.

Table 1: DFT-calculated E_{hull} of RCCAs that have been observed to form single-phase solid solution experimentally.

Composition	E_{hull}(meV/atom)	Composition	E_{hull}(meV/atom)
MoNbTi	0	HfMoNbTaTi	0
NbTaTi	0	HfMoNbTaZr	0
NbTiZr	0	HfMoNbTiZr	0
MoNbTa	12	HfMoTaTiZr	0
AlMoNbTi	0	HfNbTaTiZr	0
HfNbTaTi	0	MoNbTaTiV	0
HfNbTaZr	0	MoNbTaTiW	0
HfNbTiZr	0	MoNbTaTiZr	0
HfTaTiZr	0	MoNbTaVW	0
MoNbTaTi	0	NbTaTiVW	12
MoNbTaW	0	CrMoNbTiW	13
MoNbTiV	0	MoNbTiVZr	15
MoNbTiZr	0	AlMoNbTiV	22
MoTaTiV	0	AlMoTaTiV	33
NbTaTiV	0	NbTaTiVZr	47
NbTaTiW	0		
NbTaTiZr	0		
NbTaVW	0		
AlNbTiV	10		
NbVZrTi	50		

Appendix C. Phase prediction in NbTiZr-based RCCAs

Table 2. Phases that are included in the convex hull analysis of NbTiZr alloy.

composition	ΔH(meV/atom)	ΔS(meV/K)	Source
NbZrTi	76	-9.47E-02	model
NbZr	70	-5.97E-02	DFT
NbTi	41	-5.97E-02	DFT
ZrTi	90	-5.97E-02	DFT
Nb	0	0	mp-75
Zr	0	0	mp-131
Ti	0	0	mp-72
Ti_3Nb	82	0	mp-981232
TiNb	35	0	mp-1216634
Ti_3Nb	55	0	mp-1217091
Ti_3Nb	84	0	mp-980945
Ti_3Nb	78	0	mp-1187514
ZrNb	111	0	mp-1215202
ZrTi	88	0	mp-1215236
$ZrTi_2$	185	0	mp-1080389
$ZrTi_3$	31	0	mp-1183046
$ZrTi_2$	32	0	mp-1008568
ZrTi	79	0	mp-1215200
ZrTiNb	110	0	mp-1215185

Solid solution
element
intermetallic

Table 3. Phases that are included in the convex hull analysis of NbTiZrV alloy.

composition	ΔH(meV/atom)	ΔS(meV/K)	Source
NbVZrTi	104	-1.19E-01	model
NbVZr	149	-9.47E-02	model
NbVTi	72	-9.47E-02	model
NbZrTi	76	-9.47E-02	model
VZrTi	140	-9.47E-02	model
NbV	75	-5.97E-02	DFT
NbZr	70	-5.97E-02	DFT
NbTi	41	-5.97E-02	DFT
VZr	195	-5.97E-02	DFT
VTi	86	-5.97E-02	DFT
ZrTi	90	-5.97E-02	DFT
Nb	0	0	mp-75
V	0	0	mp-146
Zr	0	0	mp-131
Ti	0	0	mp-72
NbV_2	-59	0	[11]
Ti_3Nb	82	0	mp-981232
TiNb	35	0	mp-1216634
Ti_3Nb	55	0	mp-1217091
Ti_3Nb	84	0	mp-980945
Ti_3Nb	78	0	mp-1187514
ZrNb	111	0	mp-1215202
TiV	118	0	mp-1216646
Ti_4V	121	0	mp-1217117
ZrTi	88	0	mp-1215236
$ZrTi_2$	185	0	mp-1080389
$ZrTi_3$	31	0	mp-1183046
$ZrTi_2$	32	0	mp-1008568
ZrTi	79	0	mp-1215200
Zr_3V	216	0	mp-1188058
ZrV_2	51	0	mp-258
ZrTiNb	110	0	mp-1215185

Table 4. Phases that are included in the convex hull analysis of NbTiZrVMo alloy.

composition	ΔH(meV/atom)	ΔS(meV/K)	Source
MoNbTiVZr	32	1.39E-01	model
MoNbTiV	-26	1.19E-01	model
MoNbTiZr	9	1.19E-01	model
MoTiVZr	27	1.19E-01	model
NbTiVZr	103	1.19E-01	model
MoNbVZr	36	1.19E-01	model
MoNbTi	-53	9.47E-02	model
MoNbV	-49	9.47E-02	model
MoNbZr	14	9.47E-02	model
MoTiV	-58	9.47E-02	model
MoTiZr	4	9.47E-02	model
MoVZr	38	9.47E-02	model
NbTiV	68	9.47E-02	model
NbTiZr	66	9.47E-02	model
NbVZr	122	9.47E-02	model
TiVZr	110	9.47E-02	model
MoNb	-73	5.97E-02	DFT
MoTi	-81	5.97E-02	DFT
MoV	-102	5.97E-02	DFT
MoZr	42	5.97E-02	DFT
NbTi	35	5.97E-02	DFT
NbV	65	5.97E-02	DFT
NbZr	64	5.97E-02	DFT
TiV	52	5.97E-02	DFT
TiZr	49	5.97E-02	DFT
VZr	146	5.97E-02	DFT
Mo	0	0	mp-129
Nb	0	0	mp-75
Ti	0	0	mp-131
V	0	0	mp-146
Zr	0	0	mp-72
NbV_2	-59	0	[11]
NbMo	-74	0	mp-1220327
TiMo	701	0	mp-998968
$TiMo_2$	-88	0	mp-1216675
$TiMo_3$	-147	0	mp-1017983
VMo	343	0	mp-995205
V_3Mo	-68	0	mp-972071
Zr_4Mo	910	0	mp-1207454
$ZrMo_3$	228	0	mp-30790
$ZrMo_2$	58	0	mp-1215231
ZrMo	105	0	mp-1215206
$ZrMo_2$	-139	0	mp-2049
Ti_3Nb	82	0	mp-981232
TiNb	35	0	mp-1216634
Ti_3Nb	55	0	mp-1217091
Ti_3Nb	84	0	mp-980945
Ti_3Nb	78	0	mp-1187514
ZrNb	111	0	mp-1215202
TiV	118	0	mp-1216646
Ti_4V	121	0	mp-1217117
ZrTi	88	0	mp-1215236
$ZrTi_2$	185	0	mp-1080389
$ZrTi_3$	31	0	mp-1183046
$ZrTi_2$	32	0	mp-1008568
ZrTi	79	0	mp-1215200
Zr_3V	216	0	mp-1188058
ZrV_2	51	0	mp-258
Ti_2NbMo	3986	0	mp-1096197
$TiNb_2Mo$	4257	0	mp-1097379
NbV_2Mo	4262	0	mp-1095929
$NbVMo_2$	4455	0	mp-1096452
Nb_2VMo	4316	0	mp-1095742
Ti_2VMo	3772	0	mp-1096187
TiV_2Mo	4196	0	mp-1095882
$TiVMo_2$	4154	0	mp-1096250
$ZrTiMo_4$	-60	0	mp-1215177
ZrVMo	-115	0	mp-1215168
ZrTiNb	110	0	mp-1215185

Table 5. Phases that are included in the convex hull analysis of NbTiZrVTa alloy.

composition	ΔH(meV/atom)	ΔS(meV/K)	Source
NbTaTiVZr	102	1.39E-01	model
NbTaTiV	67	1.19E-01	model
NbTaTiZr	79	1.19E-01	model
NbTiVZr	103	1.19E-01	model
TaTiVZr	118	1.19E-01	model
NbTaVZr	110	1.19E-01	model
NbTaTi	43	9.47E-02	model
NbTaV	54	9.47E-02	model
NbTaZr	77	9.47E-02	model
NbTiV	68	9.47E-02	model
NbTiZr	66	9.47E-02	model
NbVZr	122	9.47E-02	model
TaTiV	75	9.47E-02	model
TaTiZr	97	9.47E-02	model
TaVZr	138	9.47E-02	model
TiVZr	110	9.47E-02	model
NbTa	0	5.97E-02	DFT
NbTi	35	5.97E-02	DFT
NbV	65	5.97E-02	DFT
NbZr	64	5.97E-02	DFT
TaTi	61	5.97E-02	DFT
TaV	55	5.97E-02	DFT
TaZr	109	5.97E-02	DFT
TiV	52	5.97E-02	DFT
TiZr	49	5.97E-02	DFT
VZr	146	5.97E-02	DFT
Nb	0	0	mp-75
Ta	0	0	mp-50
Ti	0	0	mp-72
V	0	0	mp-146
Zr	0	0	mp-131
NbV_2	-59	0	[11]
TaNb	8	0	mp-1217892
Ti_3Nb	82	0	mp-981232
TiNb	35	0	mp-1216634
Ti_3Nb	55	0	mp-1217091
Ti_3Nb	84	0	mp-980945
Ti_3Nb	78	0	mp-1187514
ZrNb	111	0	mp-1215202
$TaTi_3$	97	0	mp-1187256
TaTi	60	0	mp-1217887
$TaTi_3$	97	0	mp-1187253
$TaTi_3$	95	0	mp-1187250
TaV_2	-103	0	mp-567276
TaV	86	0	mp-1217812
Zr_3Ta	153	0	mp-1188053
Zr_3Ta	167	0	mp-1188024
TiV	118	0	mp-1216646
Ti_4V	121	0	mp-1217117
ZrTi	88	0	mp-1215236
$ZrTi_2$	185	0	mp-1080389
$ZrTi_3$	31	0	mp-1183046
$ZrTi_2$	32	0	mp-1008568
ZrTi	79	0	mp-1215200
Zr_3V	216	0	mp-1188058
ZrV2	51	0	mp-258
$TaTiNb_2$	4424	0	mp-1097329
TaNbV	45	0	mp-1217905
ZrTiNb	110	0	mp-1215185

Table 6. Phases that are included in the convex hull analysis of NbTiZrVCr alloy.

composition	Δ*H*(meV/atom)	Δ*S*(meV/K)	Source
CrNbTiVZr	32	1.39E-01	model
CrNbTiV	-26	1.19E-01	model
CrNbTiZr	9	1.19E-01	model
CrTiVZr	27	1.19E-01	model
NbTiVZr	103	1.19E-01	model
CrNbVZr	36	1.19E-01	model
CrNbTi	-53	9.47E-02	model
CrNbV	-49	9.47E-02	model
CrNbZr	14	9.47E-02	model
CrTiV	-58	9.47E-02	model
CrTiZr	4	9.47E-02	model
CrVZr	38	9.47E-02	model
NbTiV	68	9.47E-02	model
NbTiZr	66	9.47E-02	model
NbVZr	122	9.47E-02	model
TiVZr	110	9.47E-02	model
CrNb	-73	5.97E-02	DFT
CrTi	-81	5.97E-02	DFT
CrV	-102	5.97E-02	DFT
CrZr	42	5.97E-02	DFT
NbTi	35	5.97E-02	DFT
NbV	65	5.97E-02	DFT
NbZr	64	5.97E-02	DFT
TiV	52	5.97E-02	DFT
TiZr	49	5.97E-02	DFT
VZr	146	5.97E-02	DFT
Cr	0	0	mp-90
Nb	0	0	mp-75
Ti	0	0	mp-72
V	0	0	mp-146
Zr	0	0	mp-131
NbV2	-59	0	[11]
Nb3Cr	-74	0	mp-999446
NbCr3	701	0	mp-999392
NbCr2	-88	0	mp-1220609
NbCr3	-147	0	mp-999393
Nb3Cr	343	0	mp-999441
NbCr2	-68	0	mp-548
NbCr2	910	0	mp-1095643
NbCr2	228	0	mp-1191777
Nb2Cr	58	0	mp-1077258
NbCr3	105	0	mp-999390
Nb3Cr	-139	0	mp-999439
TiCr2	82	0	mp-1425
TiCr2	35	0	mp-568636
TiCr2	55	0	mp-1589
Ti4Cr	84	0	mp-1217156
VCr3	78	0	mp-1187696
V3Cr	111	0	mp-1187695
VCr	118	0	mp-1216394
ZrCr2	121	0	mp-570608
ZrCr2	88	0	mp-903
ZrCr2	185	0	mp-1919
Ti3Nb	31	0	mp-981232
TiNb	32	0	mp-1216634
Ti3Nb	79	0	mp-1217091
Ti3Nb	216	0	mp-980945
Ti3Nb	51	0	mp-1187514
ZrNb	3986	0	mp-1215202
TiV	4257	0	mp-1216646
Ti4V	4262	0	mp-1217117
ZrTi	4455	0	mp-1215236
ZrTi2	4316	0	mp-1080389
ZrTi3	3772	0	mp-1183046
ZrTi2	4196	0	mp-1008568
ZrTi	4154	0	mp-1215200
Zr3V	-60	0	mp-1188058
ZrV2	-115	0	mp-258
TiNbCr4	110	0	mp-1216666
NbVCr	-0.09	0	mp-1220374
ZrNbCr4	-0.04	0	mp-1215217
ZrTiCr4	-0.04	0	mp-1215221
ZrTiCr4	-0.05	0	mp-1215179
ZrVCr	-0.02	0	mp-1215170
ZrTiNb	0.11	0	mp-1215185

Appendix D. Single-phase BCC RCCAs candidates

Quaternary alloys

1000 K (meV/atom)									
Composition	E_{hull}	Composition	E_{hull}	Composition	E_{hull}	Composition	E_{hull}	Composition	E_{hull}
HfNbVZr	3	CrMoNbOs	11	CrTaTiZr	15	HfTaVZr	17	NbReVZr	19
CrMoReW	3	MoNbOsRu	11	CrHfTaTi	15	CrMoReTa	17	CrMoRhRu	19
HfNbVW	5	CrNbTaTi	11	CrMoOsV	15	CrTaTiW	17	CrHfTaV	19
HfMoNbV	7	CrMoRhW	11	HfMoNbW	16	HfNbReV	17	CrHfNbV	19
CrTaTiV	8	CrMoNbRe	11	MoNbWZr	16	CrNbReW	18	CrRuVW	20
HfTaTiV	8	CrMoReRu	12	CrMoRuV	16	CrMoNbRu	18	CrHfTiZr	20
NbVWZr	8	CrMoOsW	12	HfMoTiW	16	HfMoWZr	18	MoRhRuW	20
NbReTaZr	8	MoOsReRu	13	CrNbOsW	16	CrNbOsRu	18	MoOsRuW	20
AlCrVW	9	CrHfNbTi	14	CrMoOsTa	16	ReTaVZr	18	CrMoOsRh	20
CrReRhRu	9	CrReRhW	14	HfReTaV	16	CrReRuW	18	HfMoVW	20
MoNbVZr	10	CrMoOsRe	14	MoTiWZr	17	CrMoReV	18	HfMoTaW	20
HfNbReTa	10	CrNbTiW	15	MoOsRuV	17	CrMoTaTi	19	AlNbTiV	20
CrOsReRu	10								

2000 K (meV/atom)									
Composition	E_{hull}	Composition	E_{hull}	Composition	E_{hull}	Composition	E_{hull}	Composition	E_{hull}
CrMoOsRu	0	HfMoNbTi	9	CrNbTiZr	13	CrOsRhW	16	CrRuVW	18
CrOsRhRu	0	OsReRhRu	9	MoNbWZr	13	CrMoRuV	16	CrNbOsRu	18
HfNbTiV	0	CrMoTiW	9	CrMoNbOs	14	HfMoReZr	16	CrMoNbTi	18
NbTiVZr	0	MoOsRuV	9	CrMoOsRh	14	HfMoNbV	16	OsRhRuW	18
IrOsRhRu	2	MoNbTaTi	9	CrMoNbW	14	CrTiWZr	16	MoNbVZr	18
HfNbTaV	2	HfNbTaTi	10	CrMoVW	14	CrNbTiW	16	MoOsRhW	18
NbTaVZr	3	CrOsReRu	10	MoOsRhRu	14	MoOsRuTa	16	CrNbTaW	18
MoNbOsRu	3	MoNbTiV	10	CrReRhW	14	CrMoOsW	16	MoOsReV	19
TaTiVZr	4	MoOsReRu	10	NbTaWZr	14	IrReRhRu	16	CrMoReSi	19
NbTaTiV	4	CrMoRuW	10	CrTaTiZr	14	CrReRhRu	16	CrMoNbRu	19
CrOsRuW	4	NbTiWZr	11	CrMoOsV	14	MoReRuV	16	CrMoOsRe	19
HfNbTiZr	5	IrOsReRh	11	HfMoTiW	15	NbOsRuW	17	MoNbTiW	19
HfTaTiV	5	CrMoReRh	11	CrHfTaTi	15	IrOsReRu	17	MoOsRuW	19
CrMoReW	5	CrNbTaTi	11	MoNbTaZr	15	CrTaTiV	17	CrOsVW	19
CrMoRhW	6	NbTaVW	11	MoRhRuW	15	CrMoNbRe	17	HfTaVZr	19
HfTaTiZr	6	HfNbTiW	11	MoNbTaV	15	CrMoReRu	17	NbRuTaV	19
TaTiVW	7	HfTiVZr	11	HfNbReTa	15	HfReTaV	17	HfMoTiV	20
NbTaTiZr	8	CrIrOsRu	11	HfNbVW	15	CrNbTaZr	17	HfNbTaZr	20
NbTaTiW	8	HfNbVZr	12	CrMoWZr	15	NbVWZr	17	MoTiVZr	20

CrRhRuW	8	CrOsRuV	12	TaVWZr	15	NbReTaZr	17	MoNbTaW	20
MoTaTiV	8	HfNbTaW	12	HfMoWZr	15	CrIrRhRu	17	AlCrTaW	20
AlCrVW	8	HfMoTaV	12	MoTaVZr	15	CrNbOsW	18	CrMoTiZr	20
NbTiVW	8	HfTaVW	12	CrHfNbTi	15	AlNbTaV	18	CrOsReRh	20
CrMoRhRu	8	CrIrOsRh	13	MoTiWZr	15	AlMoVW	18	CrNbRuW	20
MoNbTiZr	8	HfMoNbTa	13	HfNbReZr	15	CrTaTiW	18	HfTiVW	20
AlCrMoW	8	HfMoNbW	13	CrMoTaW	15				

Quinary alloys

1000 K (meV/atom)									
Composition	E_{hull}	Composition	E_{hull}	Composition	E_{hull}	Composition	E_{hull}	Composition	E_{hull}
HfNbTiVZr	9	HfNbTiVW	14	HfMoNbTaTi	16	HfMoNbTiZr	17	MoNbTiVW	20
HfNbTaTiZr	12	NbTaTiWZr	15	HfMoNbTiV	16	HfTaTiVZr	18	CrIrOsRhRu	20
NbTaTiVW	13	HfNbTaTiW	15	MoNbTaTiZr	16	CrOsReRhRu	19	MoNbTaTiW	20
NbTaTiVZr	13	NbTiVWZr	15	HfNbTiWZr	17	HfNbTaVW	19	NbTaVWZr	20
HfNbTaTiV	14	MoNbTaTiV	15	MoNbTiVZr	17	IrOsReRhRu	19		

2000 K (meV/atom)									
Composition	E_{hull}	Composition	E_{hull}	Composition	E_{hull}	Composition	E_{hull}	Composition	E_{hull}
NbTaTiVZr	7	CrOsRhRuW	15	CrIrOsRhRu	17	HfNbTaVZr	18	CrMoNbTiZr	19
HfNbTaTiV	8	CrNbTaTiZr	15	CrHfNbTiZr	17	NbTaTiWZr	18	HfMoNbTaTi	19
CrMoRhRuW	11	HfNbTaTiZr	15	MoOsRhRuW	17	HfMoNbTiW	18	HfMoNbTiV	19
HfNbTiVZr	12	HfNbTaVW	15	CrOsRuVW	17	NbTiVWZr	18	MoNbTaTiZr	19
NbTaTiVW	12	CrMoNbOsRu	15	HfMoNbTaV	17	CrOsReRuW	18	HfMoTaTiV	19
CrMoOsReRu	14	CrMoOsRuV	15	IrOsReRhRu	18	CrNbTiWZr	18	MoNbTiWZr	20
CrMoOsRhRu	14	CrMoOsRhW	16	HfNbTiVW	18	HfTaTiVW	19	HfNbTiWZr	20
HfTaTiVZr	14	NbTaVWZr	16	TaTiVWZr	18	CrNbTaTiW	19	MoNbTiVZr	20
MoNbTaTiV	15	CrOsReRhRu	16	HfNbTaTiW	18	MoTaTiVZr	19	HfMoNbTiZr	20
CrMoOsRuW	15	CrNbOsRuW	17	CrHfNbTaTi	18	MoNbTaVZr	19	CrHfTaTiZr	20

Senary alloys

1000 K (meV/atom)									
Composition	E_{hull}	Composition	E_{hull}	Composition	E_{hull}	Composition	E_{hull}	Composition	E_{hull}
HfNbTaTiVZr	17	HfNbTaTiVW	17	HfMoNbTiVZr	19	HfNbTiVWZr	20	MoNbTiVW	20
NbTaTiVWZr	17	HfMoNbTaTiV	19	MoNbTaTiVZr	19				

2000 K (meV/atom)									
Composition	E_{hull}	Composition	E_{hull}	Composition	E_{hull}	Composition	E_{hull}	Composition	E_{hull}
HfNbTaTiVZr	16	CrMoOsRhRuW	17	CrHfNbTaTiZr	20	HfMoNbTaTiV	20	NbTaTiVWZr	20

Appendix E. Comparison of our model with a similar model reported by Bokas et al. [Ref. 23]

As discussed in the manuscript, our approach of using pairwise mixing enthalpies to estimate the mixing enthalpy of HEAs is similar to that proposed by Bokas et al.[23]. For the 14 elements that we have in common (Al, Ti, V, Cr, Zr, Nb, Mo, Hf, Ta, W, Re, Os, Rh, and Ir), we compare the mixing enthalpy of their ternary, quaternary and quinary alloys using both the models. The results are shown in Fig. 7. Overall, we find a good agreement between both the models with an MAE of 0.035 eV/atom between the two models. However, alloys containing Hf-Ti, Re-Mo, and Os-Mo pairs show large differences. For instance, the model by Bokas *et al.*, gives lower ΔH_{mix} predictions on HfTiV and ReMoOs compared to ours. This difference can be tracked back to the different pairwise mixing enthalpy of Hf-Ti, Re-Mo, and Os-Mo in the two models. We obtain mixing enthalpy of Hf-Ti, Re-Mo, and Os-Mo as 0.04, 0.04, and 0.11 eV/atom, respectively. For the respective pairs, Bokas et al. report values of –0.36, –0.04, and –0.21 eV/atom. These differences may arise from the different values of the cutoff energy and *k*-points used for the DFT calculations in the two studies; we have used tighter convergence settings.

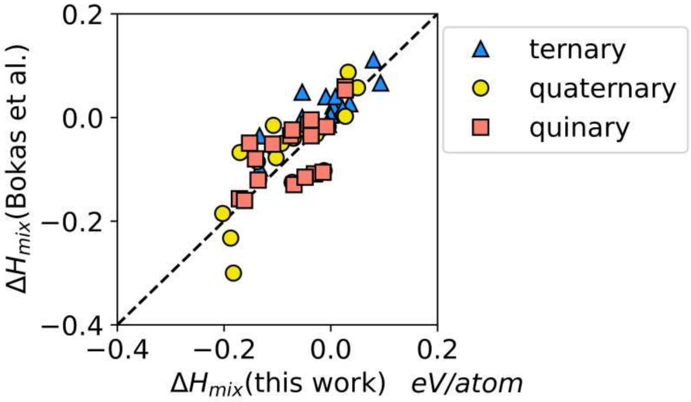

Fig. 7: A comparison of predicted ΔH_{mix} using our model and the model by Bokas et al. (Ref [23]) for ternary, quaternary and quinary alloys.

References:

[1] B. Cantor, I.T.H. Chang, P. Knight, A.J.B. Vincent, Microstructural development in equiatomic multicomponent alloys, Materials Science and Engineering: A 375-377 (2004) 213-218.

[2] J.-W. Yeh, S.-K. Chen, S.-J. Lin, J.-Y. Gan, T.-S. Chin, T.-T. Shun, C.-H. Tsau, S.-Y. Chang, Nanostructured High-Entropy Alloys with Multiple Principal Elements: Novel Alloy Design Concepts and Outcomes, Advanced Engineering Materials 6(5) (2004) 299-303.

[3] B. Gludovatz, A. Hohenwarter, K.V.S. Thurston, H. Bei, Z. Wu, E.P. George, R.O. Ritchie, Exceptional damage-tolerance of a medium-entropy alloy CrCoNi at cryogenic temperatures, Nature Communications 7(1) (2016) 10602.

[4] Z. Wu, H. Bei, G.M. Pharr, E.P. George, Temperature dependence of the mechanical properties of equiatomic solid solution alloys with face-centered cubic crystal structures, Acta Materialia 81 (2014) 428-441.

[5] F. Otto, Y. Yang, H. Bei, E.P. George, Relative effects of enthalpy and entropy on the phase stability of equiatomic high-entropy alloys, Acta Materialia 61(7) (2013) 2628-2638.

[6] C.K.H. Borg, C. Frey, J. Moh, T.M. Pollock, S. Gorsse, D.B. Miracle, O.N. Senkov, B. Meredig, J.E. Saal, Expanded dataset of mechanical properties and observed phases of multi-principal element alloys, Scientific Data 7(1) (2020) 430.

[7] O.N. Senkov, S. Rao, K.J. Chaput, C. Woodward, Compositional effect on microstructure and properties of NbTiZr-based complex concentrated alloys, Acta Materialia 151 (2018) 201-215.

[8] M. Li, Z. Zhang, A.S. Thind, G. Ren, R. Mishra, K.M. Flores, Microstructure and properties of NbVZr refractory complex concentrated alloys, Acta Materialia 213 (2021).

[9] S. Kirklin, J.E. Saal, B. Meredig, A. Thompson, J.W. Doak, M. Aykol, S. Ruhl, C. Wolverton, The Open Quantum Materials Database (OQMD): assessing the accuracy of DFT formation energies, Npj Computational Materials 1 (2015) 15.

[10] A. Jain, S.P. Ong, G. Hautier, W. Chen, W.D. Richards, S. Dacek, S. Cholia, D. Gunter, D. Skinner, G. Ceder, K.A. Persson, Commentary: The Materials Project: A materials genome approach to accelerating materials innovation, APL Mater. 1(1) (2013) 11.

[11] Z. Zhang, M. Li, K. Flores, R. Mishra, Machine learning formation enthalpies of intermetallics, Journal of Applied Physics 128(10) (2020) 105103.

[12] J. Qi, A.M. Cheung, S.J. Poon, High Entropy Alloys Mined From Binary Phase Diagrams, Scientific Reports 9(1) (2019) 15501.

[13] M.C. Troparevsky, J.R. Morris, P.R.C. Kent, A.R. Lupini, G.M. Stocks, Criteria for Predicting the Formation of Single-Phase High-Entropy Alloys, Physical Review X 5(1) (2015) 6.

[14] Y. Zhang, Y.J. Zhou, J.P. Lin, G.L. Chen, P.K. Liaw, Solid-Solution Phase Formation Rules for Multi-component Alloys, Advanced Engineering Materials 10(6) (2008) 534-538.

[15] A.R. Miedema, P.F. de Châtel, F.R. de Boer, Cohesion in alloys — fundamentals of a semi-empirical model, Physica B+C 100(1) (1980) 1-28.

[16] S. Guo, C.T. Liu, Phase stability in high entropy alloys: Formation of solid-solution phase or amorphous phase, Progress in Natural Science: Materials International 21(6) (2011) 433-446.

[17] A. Zunger, S. Wei, L.G. Ferreira, J.E. Bernard, Special quasirandom structures, Phys Rev Lett 65(3) (1990) 353-356.

[18] R. Feng, P.K. Liaw, M.C. Gao, M. Widom, First-principles prediction of high-entropy-alloy stability, npj Computational Materials 3(1) (2017) 50.

[19] C. Niu, Y. Rao, W. Windl, M. Ghazisaeidi, Multi-cell Monte Carlo method for phase prediction, npj Computational Materials 5(1) (2019).

[20] Y. Lederer, C. Toher, K.S. Vecchio, S. Curtarolo, The search for high entropy alloys: A high-throughput ab-initio approach, Acta Materialia 159 (2018) 364-383.

[21] G.L.W. Hart, R.W. Forcade, Algorithm for generating derivative structures, Physical Review B 77(22) (2008).

[22] A. Jain, S.P. Ong, G. Hautier, W. Chen, W.D. Richards, S. Dacek, S. Cholia, D. Gunter, D. Skinner, G. Ceder, K.A. Persson, Commentary: The Materials Project: A materials genome approach to accelerating materials innovation, APL Materials 1(1) (2013) 011002.

[23] G.B. Bokas, W. Chen, A. Hilhorst, P.J. Jacques, S. Gorsse, G. Hautier, Unveiling the thermodynamic driving forces for high entropy alloys formation through big data ab initio analysis, Scripta Materialia 202 (2021) 114000.

[24] E.A. Guggenheim, R.H. Fowler, The statistical mechanics of regular solutions, Proceedings of the Royal Society of London. Series A - Mathematical and Physical Sciences 148(864) (1935) 304-312.

[25] A. Zunger, Spontaneous Atomic Ordering in Semiconductor Alloys: Causes, Carriers, and Consequences, MRS Bulletin 22(7) (1997) 20-26.

[26] A.R. Natarajan, P. Dolin, A. Van der Ven, Crystallography, thermodynamics and phase transitions in refractory binary alloys, Acta Materialia 200 (2020) 171-186.

[27] A. Manzoor, S. Pandey, D. Chakraborty, S.R. Phillpot, D.S. Aidhy, Entropy contributions to phase stability in binary random solid solutions, npj Computational Materials 4(1) (2018) 47.

[28] M.D. Hossain, T. Borman, C. Oses, M. Esters, C. Toher, L. Feng, A. Kumar, W.G. Fahrenholtz, S. Curtarolo, D. Brenner, J.M. LeBeau, J.P. Maria, Entropy Landscaping of High-Entropy Carbides, Adv Mater 33(42) (2021) e2102904.

[29] S.P. Ong, W.D. Richards, A. Jain, G. Hautier, M. Kocher, S. Cholia, D. Gunter, V.L. Chevrier, K.A. Persson, G. Ceder, Python Materials Genomics (pymatgen): A robust, open-source python library for materials analysis, Computational Materials Science 68 (2013) 314-319.

[30] A. R. Akbarzadeh, V. Ozoliņš, C. Wolverton, First-Principles Determination of Multicomponent Hydride Phase Diagrams: Application to the Li-Mg-N-H System, Advanced Materials 19(20) (2007) 3233-3239.

[31] D. Evans, J. Chen, G. Bokas, W. Chen, G. Hautier, W. Sun, Visualizing temperature-dependent phase stability in high entropy alloys, npj Computational Materials 7(1) (2021) 151.

[32] J. Cavin, A. Ahmadiparidari, L. Majidi, A.S. Thind, S.N. Misal, A. Prajapati, Z. Hemmat, S. Rastegar, A. Beukelman, M.R. Singh, K.A. Unocic, A. Salehi-Khojin, R. Mishra, 2D High-Entropy Transition Metal Dichalcogenides for Carbon Dioxide Electrocatalysis, Adv Mater 33(31) (2021) 2100347.

[33] Z. Hemmat, J. Cavin, A. Ahmadiparidari, A. Ruckel, S. Rastegar, S.N. Misal, L. Majidi, K. Kumar, S. Wang, J. Guo, R. Dawood, F. Lagunas, P. Parajuli, A.T. Ngo, L.A. Curtiss, S.B. Cho, J. Cabana, R.F. Klie, R. Mishra, A. Salehi-Khojin, Quasi-Binary Transition Metal Dichalcogenide Alloys: Thermodynamic Stability Prediction, Scalable Synthesis, and Application, Advanced Materials 32(26) (2020) 1907041.

[34] H.-W. Luan, Y. Shao, J.-F. Li, W.-L. Mao, Z.-D. Han, C. Shao, K.-F. Yao, Phase stabilities of high entropy alloys, Scripta Materialia 179 (2020) 40-44.

[35] J. Cavin, R. Mishra, Equilibrium Phase Diagrams of Isostructural and Heterostructural Two-Dimensional Alloys from First Principles, ISCIENCE (2022).

[36] A. Zunger, S. Wei, L.G. Ferreira, J.E. Bernard, Special quasirandom structures, Phys. Rev. Lett. 65(3) (1990) 353-356.

[37] A. van de Walle, M. Asta, G. Ceder, The Alloy Theoretic Automated Toolkit: A user guide, Calphad 26(4) (2002) 539-553.

[38] Z. Zhang, M-cube, M-cube-wustl/RHEAs_phase_prediction https://doi.org/10.5281/zenodo.6380713, (2022).

[39] G. Kresse, J. Furthmuller, Efficient iterative schemes for ab initio total-energy calculations using a plane-wave basis set, Phys Rev B Condens Matter 54(16) (1996) 11169-11186.

[40] J.P. Perdew, K. Burke, M. Ernzerhof, Generalized Gradient Approximation Made Simple, Phys Rev Lett 77(18) (1996) 3865-3868.

[41] P.E. Blochl, Projector augmented-wave method, Phys Rev B Condens Matter 50(24) (1994) 17953-17979.

[42] M. Li, J. Gazquez, A. Borisevich, R. Mishra, K.M. Flores, Evaluation of microstructure and mechanical property variations in AlxCoCrFeNi high entropy alloys produced by a high-throughput laser deposition method, Intermetallics 95 (2018) 110-118.

[43] M. Li, Z. Zhang, A.S. Thind, G. Ren, R. Mishra, K.M. Flores, Microstructure and properties of NbVZr refractory complex concentrated alloys, Acta Materialia 213 (2021) 116919.

[44] A. Jain, G. Hautier, C.J. Moore, S. Ping Ong, C.C. Fischer, T. Mueller, K.A. Persson, G. Ceder, A high-throughput infrastructure for density functional theory calculations, Computational Materials Science 50(8) (2011) 2295-2310.

[45] A. Jain, G. Hautier, S.P. Ong, C.J. Moore, C.C. Fischer, K.A. Persson, G. Ceder, Formation enthalpies by mixing GGA and GGA $+$ U calculations, Physical Review B 84(4) (2011) 045115.

[46] S. Curtarolo, W. Setyawan, G.L.W. Hart, M. Jahnatek, R.V. Chepulskii, R.H. Taylor, S.D. Wanga, J.K. Xue, K.S. Yang, O. Levy, M.J. Mehl, H.T. Stokes, D.O. Demchenko, D. Morgan, AFLOW: An automatic framework for high-throughput materials discovery, Computational Materials Science 58 (2012) 218-226.

[47] W. Kucza, J. Dąbrowa, G. Cieślak, K. Berent, T. Kulik, M. Danielewski, Studies of “sluggish diffusion” effect in Co-Cr-Fe-Mn-Ni, Co-Cr-Fe-Ni and Co-Fe-Mn-Ni high entropy alloys; determination of tracer diffusivities by combinatorial approach, Journal of Alloys and Compounds 731 (2018) 920-928.

[48] Z. Leong, U. Ramamurty, T.L. Tan, Microstructural and compositional design principles for Mo-V-Nb-Ti-Zr multi-principal element alloys: a high-throughput first-principles study, Acta Materialia 213 (2021) 116958.

[49] We selected Ti over other elements due to the availability of high-quality Ti powder for the laser-based deposition experiments.

[50] W. Sun, T. Dacek Stephen, P. Ong Shyue, G. Hautier, A. Jain, D. Richards William, C. Gamst Anthony, A. Persson Kristin, G. Ceder, The thermodynamic scale of inorganic crystalline metastability, Science Advances 2(11) e1600225.

[51] D.B. Miracle, M. Li, Z. Zhang, R. Mishra, K.M. Flores, Emerging Capabilities for the High-Throughput Characterization of Structural Materials, Annual Review of Materials Research (2021).

[52] M. Li, J. Gazquez, A. Borisevich, R. Mishra, K.M. Flores, Evaluation of microstructure and mechanical property variations in Al x CoCrFeNi high entropy alloys produced by a high-throughput laser deposition method, Intermetallics 95 (2018) 110-118.

[53] J. Cavin, R. Mishra, Equilibrium phase diagrams of isostructural and heterostructural two-dimensional alloys from first principles, iScience 25(4) (2022).

[54] Z. Hemmat, J. Cavin, A. Ahmadiparidari, A. Ruckel, S. Rastegar, S.N. Misal, L. Majidi, K. Kumar, S. Wang, J. Guo, R. Dawood, F. Lagunas, P. Parajuli, A.T. Ngo, L.A. Curtiss, S.B. Cho, J. Cabana, R.F. Klie, R. Mishra, A. Salehi-Khojin, Quasi-Binary Transition Metal Dichalcogenide Alloys: Thermodynamic Stability Prediction, Scalable Synthesis, and Application, Adv Mater 32(26) (2020) 1907041.

[55] M. Widom, W.P. Huhn, S. Maiti, W. Steurer, Hybrid Monte Carlo/Molecular Dynamics Simulation of a Refractory Metal High Entropy Alloy, Metallurgical and Materials Transactions A 45(1) (2013) 196-200.

[56] E. Antillon, M. Ghazisaeidi, Efficient determination of solid-state phase equilibrium with the multicell Monte Carlo method, Phys Rev E 101(6-1) (2020) 063306.

[57] R.-C.T. Ming-Huang Tsai, Ting Chang, Wei-Fei Huang, Intermetallic Phases in High-Entropy alloys: Statistical Analysis of their Prevalence and Structural Inheritance, Metals (2019).

[58] D.B. Miracle, O.N. Senkov, A critical review of high entropy alloys and related concepts, Acta mater. 122 (2017) 448-511.

[59] D. Ma, B. Grabowski, F. Körmann, J. Neugebauer, D. Raabe, Ab initio thermodynamics of the CoCrFeMnNi high entropy alloy: Importance of entropy contributions beyond the configurational one, Acta Materialia 100 (2015) 90-97.

[60] M. Widom, Prediction of Structure and Phase Transformations, in: M.C. Gao, J.-W. Yeh, P.K. Liaw, Y. Zhang (Eds.), High-Entropy Alloys: Fundamentals and Applications, Springer International Publishing, Cham, 2016, pp. 267-298.

[61] D.B. Miracle, O.N. Senkov, A critical review of high entropy alloys and related concepts, Acta Materialia 122 (2017) 448-511.

[62] L.-F. Huang, X.-Z. Lu, E. Tennessen, J.M. Rondinelli, An efficient ab-initio quasiharmonic approach for the thermodynamics of solids, Comp Mater Sci 120 (2016) 84-93.